Journal of Bio- and Tribo-Corrosion (2022) 8:98
https://doi.org/10.1007/s40735-022-00700-1

Additive Manufacturing of Ti-6Al-4V alloy for Biomedical Applications

Yashwanth Kumar Balasubramanian Gayathri[1,2] · R. Lokesh Kumar[1,2] · Vaira Vignesh Ramalingam[1] · G. Suganya Priyadharshini[3] · K. Santhosh Kumar[1] · T. Ram Prabhu[4]

Received: 17 March 2022 / Revised: 15 July 2022 / Accepted: 17 August 2022 / Published online: 28 August 2022

Abstract

Ti-6Al-4V alloy is one of the widely used titanium alloys for biomedical applications, especially in load-critical bio-implants, because of its high strength, biocompatibility, and corrosion resistance. However, conventional manufacturing processes pose many challenges for the fabrication and processing of Ti-6Al-4V alloy-based implants. The emerging additive manufacturing technologies, particularly selective laser melting, provide an ideal platform for manufacturing customized and complex-geometry implants with high-dimensional accuracy. This study evaluates the mechanical properties, and bio-corrosion resistance of selective laser melted Ti-6Al-4V alloy. The microstructural analysis showed the presence of a continuous networked structure of the β phase, which paved the way for an ample microhardness of 255 HV. A comprehensive analysis of the fracture mechanism and bio-corrosion mechanism of the selective laser melted Ti-6Al-4V alloy is presented. The fractography depicted a combination of ductile and brittle fracture mechanisms, resulting in a fair ultimate tensile strength value of 813 MPa. Meanwhile, the formation of calcium hydroxyapatite in the course of corrosion during the implantation period helps in bone growth and promotes implant–bone stability. The corrosion rate of the SLM Ti-6Al-4V alloy in simulated body fluid was 9×10^{-4} mm/year. The results provide a new avenue to fabricate selective laser melted Ti-6Al-4V alloy with desired mechanical properties and bio-corrosion resistance.

✉ Vaira Vignesh Ramalingam
r_vairavignesh@cb.amrita.edu

Yashwanth Kumar Balasubramanian Gayathri
bgyashwanth2000@gmail.com

R. Lokesh Kumar
lokeshkumarranganathan@gmail.com

G. Suganya Priyadharshini
suganyapriyadharshini.g@cit.edu.in

K. Santhosh Kumar
santhosh532000@gmail.com

[1] Department of Mechanical Engineering, Amrita School of Engineering, Amrita Vishwa Vidyapeetham, Coimbatore, India

[2] Department of Mathematics and Physics, School of Mathematics and Physics, Queens University, Belfast, UK

[3] Department of Mechanical Engineering, Coimbatore Institute of Technology, Anna University, Coimbatore, India

[4] CEMILAC, Defence Research and Development Organization, Bengaluru, India

Graphical abstract

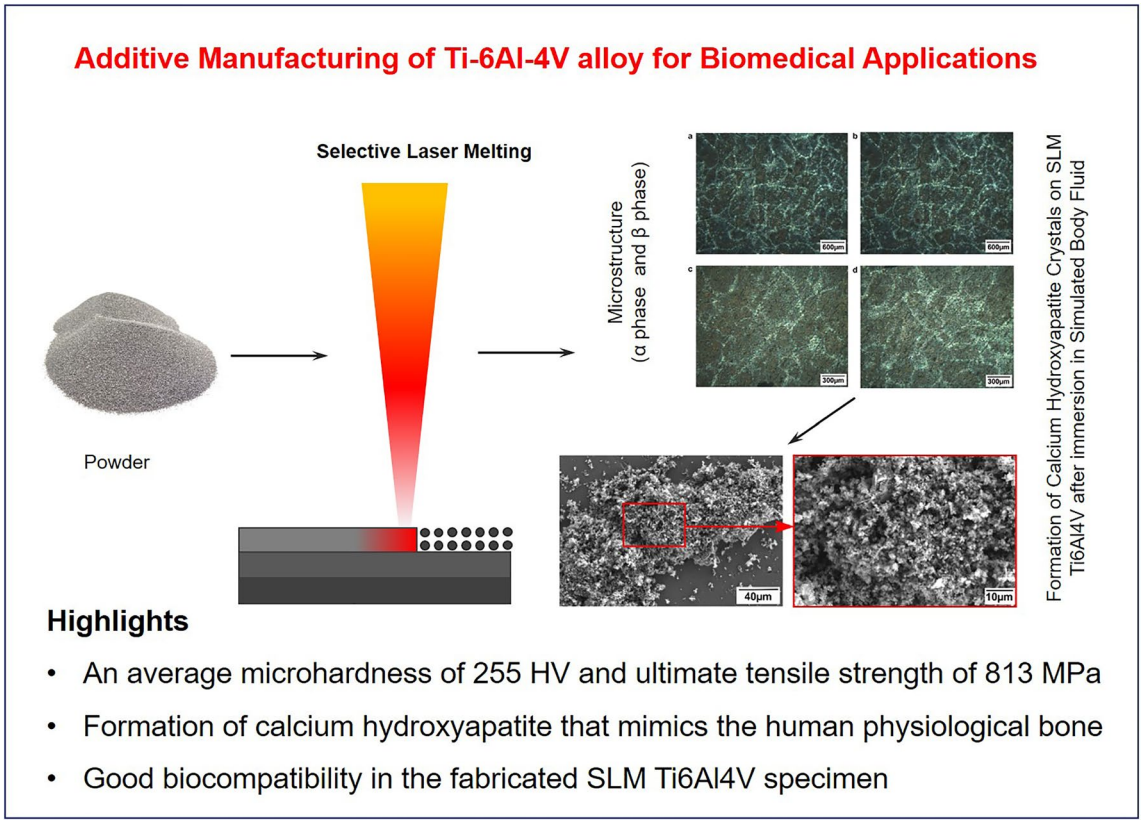

Keywords Additive manufacturing · Selective laser melting · Ti-6Al-4V · Bio-corrosion · Implants

1 Introduction

Medical implants are devices that support or replace the damaged or misplaced biological structure. One of the prime necessities of implant material includes demonstrating a good compatible index in a human biological environment. Also, the implant material should sustain the diverse biological responses while meeting adequate functional requirements [1]. The implant material should have a favorable elastic modulus of 18 GPa, comparable to human cortical bones. The geometrical design and physio-mechanical properties of the implant material should ensure uniform stress distribution and high tensile and compressive strengths to avoid fracture. The implant materials must demonstrate adequate fatigue properties under cyclic loading conditions. Also, the implant materials should possess a suitable hardness index, toughness, and wear resistance.

The suitable implant materials for permanent or prolonged contact with tissue, bone, or blood include stainless steel, cobalt-chromium alloys, magnesium-based alloys, nickel–chromium alloys, titanium-based alloys, and some alloys of tantalum and gold [2–4]. Titanium alloys are preferred for superior strength, strength-to-weight ratio, corrosion resistance, heat resistance, and biocompatibility [5]. Titanium is alloyed by adding elements such as Ag, Al, Cu, Fe, Ur, Va, and Zn. Titanium alloys can be classified into four categories: α alloys, near α alloys (small amount of beta), $\alpha+\beta$ alloys, and β alloys. Ti-5Al-2.5Sn, Ti-2Al-2Sn-4Zr-2Mo, Ti-6Al-4V, and Ti-13V-11Cr-3Al are examples of α alloy, near α alloy, $\alpha+\beta$ alloy, and β alloy, respectively [6]. Among titanium alloys, Ti-6Al-4V (6% Al, 4% V, and rest Ti) is one of the most suitable alloys for biomedical implants [7–10]. Ti-6Al-4V showed good resistance to corrosion and had excellent mechanical properties [5, 11, 12]. Ti-6Al-4V alloy could be fabricated through casting, forging, rolling, powder metallurgy, foaming technology, and other conventional methods [13]. Generally, medical implants are fabricated to suit the individual requirements of the patients or the adoption of surgical methods. Hence, adopting conventional processing techniques for fabricating Ti-6Al-4V alloy-based medical implants is a cumbersome decision. Hence, the utilization

of advanced fabrication methodologies or technologies becomes essential for the economical fabrication of medical implants with no compromise on the inherent properties of the material [14].

Additive manufacturing (AM) is a unique fabrication technology that involves the layer-by-layer addition of materials to develop components with complex geometries. Besides, intricate geometries could be developed with limited consumption of resources (less material wastage) in AM methods [15]. Also, AM methods are capable of fabricating components in a short period using digital means [16]. AM allows flexibility in design and enables the economical fabrication of unique components, even at low volumes. Hence, AM can be effectively employed for the economical fabrication of unique medical implants with desirable properties and increased "design freedom" [17, 18].

The additive manufacturing methods are categorized based on material phase change, operating principle, and modeling methods. AM methods primarily include laser-based, melt extrusion, material jetting, material adhesion, and electron beam processes [19]. Processes like selective laser melting and electron beam melting are the most suitable metal additive manufacturing process [20]. Selective Laser Melting (SLM), a LASER-based AM technology, fabricates sound components devoid of any defects.

In the SLM process, the laser heats the contour layer of metal powder that is uniformly laid on the bed. The intense heating effect melts and subsequently solidifies the metal in the desired contour layer. The process would be continued to accumulate layers to form the complex three-dimensional object. The SLM process provides better results than the direct energy deposition process [21]. However, process parameters such as build time, laser rate, laser speed, and build orientation influence the microstructural evolution and properties of the component fabricated through the SLM process [22]. Some of the literature on the properties of additive manufacturing of Ti-6Al-4V alloys is discussed below.

Tuomi et al. [23] studied in-vitro cytotoxicity and surface topography of additively manufactured Ti-6Al-4V alloy for patient-specific implant purposes. The specimens were designed and fabricated using direct metal laser sintering (DMLS) and electron beam melting (EBM). The EBM processed specimen's surface roughness (Ra 29.94) was higher than DMLS (Ra 7.867) processed specimens. The cell viability of the EBM and DMLS processed specimens was 77.4–89.7%. Sharma et al. [24] investigated the electrochemical corrosion behavior of SLM processed Ti-6Al-4V specimens in different electrolytes. The microstructure of SLM processed Ti-6Al-4V specimens revealed the presence of abundant α' martensite phases with high surface porosity. Ti-6Al-4V alloy showed high corrosion resistance in NaOH solution ($I_{Corr} = 1.798$ μA/cm^2 and $E_{Corr} = -0.382$ V) and least corrosion resistance in H_2SO_4 solution ($I_{Corr} = 5.04$ μA/cm^2 and $E_{Corr} = -0.702$ V). Yang et al. [25] studied the effect of SLM process parameters (scanning velocity between 600 and 1100 mm/s and hatch spacing between 70 and 120 μm) on the martensitic phase of Ti-6Al-4V alloy. Microstructure revealed martensite structures with a high density of dislocations. Also, twins with primary, secondary, tertiary, and quartic α' martensites within columnar β grains were observed. The martensitic sizes increased with an increase in hatch spacing. However, the martensitic sizes decreased with an increase in scanning velocity from 600 to 1100 mm/s. Hence, martensitic sizes can be controlled by selecting suitable process parameters in the SLM process.

Similarly, Mierzejewska et al. [32] investigated the effect of laser beam speed on microstructure and mechanical properties of Ti-6Al-4V fabricated by the SLM process. Microstructural observation revealed the presence of the α' martensite phase due to rapid cooling. The low laser beam speed increased power density and evaporation of particles, causing a rough surface. High laser speed resulted in insufficient energy resulting in improper melting. The lowest porosity, sufficient energy density, and best surface quality were obtained for the optimum laser speed range of 500 to 700 mm/s. The evolved microstructure after heat treatment was comprised of the $\alpha + \beta$ phase. After heat treatment, the tensile strength and yield strength decreased by 20.2% and 28.2%, respectively.

Sun et al. [34] studied the effect of bulk energy density on the microstructure of SLM processed Ti-6Al-4V alloy. Processing specimens with a bulk energy density of 25 J/mm^3 caused disordered solidification. The processing of Ti-6Al-4V alloy at bulk energy density ranging from 45 to 60 J/mm^3 showed fewer defects and martensitic phases. Hence, it was preferred for fabrication. The increase in bulk energy density depicted a successive microstructural transformation: ultrafine zigzag martensite α', fine acicular martensite α', coarsened lamellar α. The martensitic phase constituted substructures which include: primary, secondary, tertiary, quartic α' phases and rods or dots α. The various martensitic substructures were attributed to thermal cycles during SLM processing.

The implementation of heat treatments influences the microstructural modification in AM Ti-6Al-4V alloy [26]. Chandramohan et al. [27] studied the effect of heat treatment on the wear and corrosion behavior of SLM Ti-6Al-4V alloy specimens. The specimens were fabricated in vertical (V) and horizontal (H) directions. Heat treatments were performed using a horizontal carbolite tube furnace. The first set of specimens (HT-1) was heat-treated to 1100 ℃ (above β transus temperature) at a rate of 5 ℃/min, withheld for 1 h, followed by cooling at the rate of 0.09 ℃/s. The second set of specimens (HT-2) was heated to 900 ℃ (below β transus temperature) at rate of 5 ℃/min, held for 1 h and followed by

cooling at a rate of 0.09 ℃/s and further followed by heating to 650 ℃, again held for 3 h which was then cooled. HT-2 specimens showed grain refinement with grain size ranging from 2.03 to 3.89 µm, whereas HT-1 specimens showed grain growth from 4.03 to 9.42 µm. Rotary wear tests were performed under varying loads of 5 N, 15 N, and 25 N at a sliding velocity of 25 m/s. Wear volume loss was less in HT-2 specimens attributed to grain refinement. Hence oxide debris was present in HT-2 (V) specimens. Corrosion behavior was observed in 1 M H_2SO_4, 1 M HCl, and 3.5% NaCl solutions. A sharp positive difference of open circuit potential (OCP) was observed in 1 M H_2SO_4 solution. The OCP of SLM Ti-6Al-4V alloy was − 0.6 V, which was improved to 0.069 V in HT-1 (V) and 0.089 V in HT-2 (H) specimens. Hence it was concluded that heat treatment (in both H and V specimens) improved corrosion resistance of SLM processed specimens' manifold.

Longhitano et al. [28] analyzed the effect of heat treatment on microstructure, and corrosion properties of Ti-6Al-4V ELI alloy fabricated using the SLM method. The specimens were heat-treated to a temperature range of 650–1050 ℃. The microstructure after heat treatment revealed the presence of α/α' phases, acicular crystals of α'/α phases with β phase, and lamellar structure of $\alpha+\beta$ phases. It was observed that after heat treatment, nucleation and growth of β phases increased the corrosion resistance in Ti-6Al-4V alloy. Comparatively, the SLM processed specimens showed high corrosion rate (anodic potential) in phosphate-buffered saline solution (E_{corr} ranging from − 0.20 to − 0.27 V) than the commercial titanium alloy (− 0.149 V). Anodizing has been implemented on SLM processed specimens (cathodic potential ranging from − 0.11 to 0.23 V) to overcome this. This anodizing process equalized the corrosion rate of SLM processed specimen with commercially pure titanium alloy.

Tsa et al. [29] studied the influence of heat treatment on the microstructural evolution and mechanical properties of Ti-6Al-4V alloy fabricated through the SLM method. The heat treatment at 600ºC reduced tensile strength and yield strength from 1362 to 1180 MPa and 1311 MPa to 1115 MPa, respectively. However, heat treatment enabled the microstructural transition from the α' phase to the $\alpha+\beta$ phase, eliminated residual stresses, and increased ductility. On the other hand, heat treatment at 800 ℃ decreased ductility due to plate-like α' phases with dislocations. As per Kusano et al., the corrosion properties of Ti-6Al-4V can be improved by heat treatment [30].

Yan et al. [13] presented a comparative study on the microstructure and mechanical properties of Ti-6Al-4V alloy fabricated by SLM and sintering methods. The microstructure analysis of SLM processed specimens revealed the presence of β grains with lath α and lamellar $\alpha+\beta$ structure. The Ti-6Al-4V alloy specimens sintered below β transus temperature indicated Widmanstätten and lamellar $\alpha+\beta$ structure. The SLM processed specimens reported high tensile strength (1152 MPa), high yield strength (946 MPa), and ductility (4.4%). The sintered specimen's tensile strength and yield strength were 931 MPa and 847 MPa, respectively. The presence of needle shape α' phases in SLM processed alloy was responsible for high strength and hardness.

Shunmugavel et al. [33] compared the mechanical properties and machinability of wrought and SLM processed Ti-6Al-4V alloy. The microstructure of wrought alloy consisted of equiaxed α grains with β grains along grain boundaries. In contrast, SLM processed specimens had lamellar microstructure of prior β grains. The yield and tensile strength of SLM processed specimens were (964 MPa) 1.6% and (1041 MPa) 4.7% higher than wrought material (yield strength-948 MPa and tensile strength-994 MPa), respectively. The hardness of SLM processed specimens and wrought alloy was 306 HV and 356 HV, respectively. After machining, the surface roughness was lesser in the SLM processed specimens (0.673 Ra for cutting speed 180 m/min). The wrought specimens showed comparatively high roughness due to high plastic flow while machining (Ra 0.783 for cutting speed 180 m/min).

Zhou et al. [11] compared the mechanical and corrosion behavior of SLM processed Ti-13Nb-13Zr alloy, commercially pure Ti, and Ti-6Al-4V alloy. Microstructure analysis revealed the presence of primary β phase with acicular martensitic α' phase in Ti-13Nb-13Zr alloy, martensitic α' phase in commercially pure Ti, and martensitic α' with less β phase in Ti-6Al-4V alloy. The *f factor* describes the ratio of mechanical property (tensile strength/elastic modulus). The highest f was reported in Ti-13Nb-13Zr (15.22). In contrast, the f value for commercially pure Ti and Ti-6Al-4V alloy was 9.90 and 12.47, respectively. The corrosion potential was reported stating commercially pure Ti with − 0.579 V, Ti-6Al-4V with − 0.639, and Ti-13Nb-13Zr with − 0.556 V. It was concluded that SLM Ti-13Nb-13Zr showed noble corrosion potential than commercially pure Ti and Ti-6Al-4V alloy. However, the corrosion was higher than the commercially pure Ti and Ti-6Al-4V alloy.

Ettefagh et al. [31] experimented with the corrosion behavior of as-fabricated and annealed Ti-6Al-4V fabricated by the SLM method. The results revealed that as-fabricated specimens had a corrosion rate 16 times higher than that of pure titanium. As a result of heat treatment at 800 ℃ for 2 h, the corrosion behavior of the as-fabricated specimens was equalized to the corrosion rate of pure titanium. Also, the residual stresses of martensitic phases were revealed through the formation of β phases. Hence heat treatment increased the corrosion resistance of the as-fabricated specimens.

The literature survey summarized the following points: The cell viability was more in direct metal laser sintering of Ti-6Al-4V (DMLS) than in Electron beam melting (EBM).

The microstructure of Ti-6Al-4V was controlled through heat treatments (annealing) or variation in process parameters (increased scanning rate, reduced hatch spacing, optimum laser speed of 500–700 mm/s, and optimum bulk energy density). The literature survey helped to realize that the corrosion resistance was improved by heat treatment or anodizing process. The transformation of martensitic α' phases to a combination of $\alpha+\beta$ phase resulting from heat treatment was responsible for better corrosion resistance. Also, from the literature, it was evident that Ti-6Al-4V resulted in less corrosion rate than TI-13Nb-13Zr. In addition, the SLM Ti-6Al-4V specimen's surface was less rough after machining than the wrought Ti-6Al-4V specimen. Other sintering methods were used to fabricate Ti-6Al-4V, but SLM specimens showed higher strength.

The literature survey also clears that one of the promising and emerging process technologies for Ti-6Al-4V alloy includes selective laser melting (additive manufacturing). Hence, an imminent scope exists for improving the quality (mechanical and corrosion) of Ti-6Al-4V alloy-based biomedical implants fabricated through selective laser melting. However, corrosion characteristics of SLM Ti-6Al-4V alloy for biomedical applications are seldom discussed in the open literature, paving the way for the research gap in this study.

In this study, the Ti-6Al-4V alloy powders of specification AMS 4928 are selective laser melted using a laser source of 200 W. The microstructure, tensile strength, and microhardness of the SLM Ti-6Al-4V alloy were investigated. Also, the immersion corrosion and electrochemical corrosion of the SLM Ti-6Al-4V alloy in simulated body fluids were evaluated. The microstructural evolution, fractography, and corrosion mechanism of the SLM Ti-6Al-4V alloy were discussed comprehensively using advanced instrumental characterization techniques (high-resolution scanning electron microscope, energy dispersive X-ray spectroscope, and X-ray diffractometer).

2 Materials and Methods

2.1 Materials

Ti-6Al-4V alloy powder, in line with the specification of ISO5832-3 standard, was used in this work. The average particle size of the Ti-6Al-4V alloy powder is 20 µm. The composition of the Ti-6Al-4V powder is given in Table 1.

2.2 Selective laser melting

The specimen was fabricated using the SLM AM machine EOSINT M270. The laser beam was emitted through an F-theta optical lens whose focus diameter was 40 µm. The processing parameters were as follows: laser power of 200 W, hatch spacing of 100 µm, layer height of 50 µm, and scanning speed of 900 mm/s. The laser movement drew a pattern, turning 45° between layers. An argon shield atmosphere was used as a protective gas. Pure argon gas with a flow rate of 35 L/min was used for shielding. The oxygen level was maintained at 0.1% in the build chamber.

2.3 Microstructure

The microstructure of the additive manufactured specimen was examined along the transverse section of the specimen. The specimens were prepared by the standard metallographic method. The polished specimens were cleaned using acetone and etched for 10 s using Kroll's reagent (94 ml of H_2O, 4 ml of con.HNO_3, and 1.5 ml of HF). The microstructure was observed in an optical microscope (Make: Carl Zeiss; Model: Axiovert 25).

2.4 Microhardness

The specimen was prepared as per the description in the previous section. The Vicker's microhardness was measured along the transverse section using the microhardness tester with a diamond indenter (Make: Mitutoyo, Model: MVK-H1), as per the standard ASTM E384. The load applied was 4.905 N (500 gf) for 15 s. An average of ten microhardness measurements was reported.

2.5 Tensile test

Three tensile test specimens were extracted from the SLM Ti-6Al-4V alloy. The specimens were tested for tensile properties as per the standard ISO 6892-1. The specimens were tested using a computerized universal tensile testing machine (Make: Tinius Olsen, Model: H25KT). Tensile tests were performed at a crosshead speed of 0.1 mm/min to determine the tensile properties and the fracture mode.

Table 1 Composition of Ti-6Al-4V alloy

Alloy	Al	Fe	C	V	O	N	Ti
TI-6Al-4V	6.315	0.15	0.018	4.075	0.18	0.007	Balance

2.6 Corrosion test

2.6.1 Immersion corrosion test

Twelve specimens of dimension 10 mm × 10 mm were cut from the additively manufactured specimen. The specimens were polished as per the description in the microstructure section. The specimens were cleaned and degreased with ethanol. The immersion corrosion test was conducted as per the standard ISO 10993-15. The specimens were weighed using a digital weighing balance (precision 0.0001 g). The immersion tests were performed in Dulbecco's phosphate-buffered solution, one of the standard simulated body fluid solutions. The composition of Dulbecco's phosphate-buffered solution is in Table 2 [35, 36]. The pH of the solution was measured with a pH meter of sensitivity ± 0.01. The temperature of the solution was maintained at 37 ± 0.1 ℃ using a digital thermostatic water bath to mimic the human physiological environment. The specimens were divided into four batches, each consisting of three specimens. The first batch of specimens was removed after 24 h of immersion.

Similarly, second, third, and fourth batch specimens were removed after an immersion period of 72 h, 120 h, and 168 h, respectively. Then, the corrosion products were removed. The specimens were weighed in a precision balance to calculate the mass loss. The corrosion rate was calculated using Eq. (1).

$$\text{Corrosion rate} = \frac{K \times \Delta M}{A \times T \times D} \tag{1}$$

where K is a constant with a value of 8.76×10^4, ΔM is the mass loss, A is the surface area, T is time, and D is the density of Ti-6Al-4V alloy.

2.6.2 Electrochemical Corrosion Test

The specimen of dimension 50 mm × 10 mm × 4 mm was cut from the SLM Ti-6Al-4V alloy. The parted specimen was polished as per ASTM E3-11 standard and prepared for electrochemical corrosion test. The specimen was isolated using insulation tape, leaving an exposure area of 0.5 mm^2 for the electrochemical corrosion test. The SLM processed specimens were immersed in Dulbecco's phosphate-buffered solution, and the characteristic corrosion parameters, including corrosion current and potential, were obtained through a potentiodynamic polarization test. An Electrochemical corrosion test was performed in an electrochemical workstation (Make: CH Instruments, Model: 680 Amp Booster). The corrosion test was carried out at a temperature of 37 ± 0.1 ℃. A thermostatic water bath was used to maintain the temperature and mimic the human physiological environment. The corrosion setup comprised 3 electrodes, namely: a working electrode (the test specimen), a reference electrode (Ag/AgCl electrode), and the counter electrode (platinum rod). The specimen was polarized in the potential range of − 1.1 to − 0.1 V with a scan rate of 5 mV/s. The current sensitivity of 10^{-2}μA was selected [37]. Eqs. (2) and (3) were used to calculate the corrosion current and corrosion rate, respectively.

$$i_{\text{corr}} = \frac{\beta_a \times \beta_c}{2.3(\beta_a + \beta_c)} \times \frac{1}{R_{\text{p}}} \tag{2}$$

$$\text{corrosion rate} = \frac{k \times i_{\text{corr}} \times E'}{A \times \rho} \tag{3}$$

where β_a is the anodic slope, β_c is the cathodic slope, R_{p} is the polarization resistance in Ω (ohms), k is constant (3272), i_{corr} is the corrosion current in Ampere, E' is the equivalent weight in grams, A is the exposed area in cm^2, and ρ is the density of the material of the specimen in g cm^{-3}[35, 38].

2.7 Characterization using Analytical Instruments

The surface morphology of the corroded SLM Ti-6Al-4V alloy specimens was observed using a high-resolution scanning electron microscope (SEM) (Make: Zeiss Sigma). The corroded products were analyzed using an energy dispersive X-ray electron spectroscope (Make: Bruker). The presence of primary and secondary components in the SLM Ti-6Al-4V alloy specimen was observed using an

Table 2 Chemical composition of Dulbecco's phosphate-buffered solution

S. No.	Solution name	Chemical formula	Concentration mg l^{-1}
1	Anhydrous calcium chloride	$CaCl_2$	100
2	Anhydrous magnesium chloride	$MgCl_2$	47
3	Potassium chloride	KCl	200
4	Potassium phosphate monobasic	KH_2PO_4	200
5	Sodium chloride	NaCl	8000
6	Anhydrous sodium phosphate dibasic	Na_2HPO_4	1150

X-ray diffractometer (Make: Rigaku; Model: Ultima IV). The XRD spectra were generated by scanning continuously at a scan rate of 0.5°/min using copper Kα radiation.

3 Results and Discussion

3.1 Microstructural Observation

The existence of more than one physical form in a chemical element is known as allotropy. This characteristic behavior is observed in titanium. Titanium transforms its crystal structure from HCP (α phase) to BCC (β phase) when the temperature exceeds 880ºC. Ti-6Al-4V is one of the α–β combination alloys with a composition of 6 wt. % aluminum (stabilizes α phase) and 4 wt. % vanadium (stabilizes β phase). The microstructure of the conventionally fabricated Ti-6Al-4V alloy depicts a clear distinction between α and β phases. A similar microstructural observation was noted in the SLM Ti-6Al-4V alloy, as observed in earlier research work [39]. Figure 1a–d shows the continuous networked structure of the β phase. The etched specimen viewed in the optical microscope indicated the presence of dark regions (α phase) and bright regions (β phase and the transformed β phase). The x-ray diffraction of the SLM Ti-6Al-4V alloy specimen indicated the presence of peaks constituting the primary phase (α) with a high relative density, as shown in Fig. 1e. The microstructural constituents of the SLM Ti-6Al-4V alloy specimen were almost similar to that of the conventionally fabricated specimen reported in the previous literature. However, the size, shape, and morphology of the phases were unique. The secondary phase (β) peaks with low relative density were detected throughout the 2θ range.

3.2 Microhardness

The microhardness was measured along the traverse section of the SLM Ti-6Al-4V alloy specimen. The average of five measurements was determined as 255.16 HV. The standard error value for hardness was found to be 5.1028 HV. The standard error value was less than 3% of the original value. The earlier research indicates that the average microhardness of the conventionally fabricated Ti-6Al-4V alloy specimen was 334 $HV_{0.5\ kg,}$ and that of pure titanium metal was 187 HV [40]. The results show that the microhardness of the SLM Ti-6Al-4V alloy specimen was higher than pure titanium metal. The fabricated additive manufactured Ti-6Al-4V specimen was not dense enough and had high porosity compared to conventional casting. Therefore, the conventional casting has a slight increase in hardness.

3.3 Tensile Strength

The room temperature tensile strength test along a longitudinal direction was performed, and ultimate tensile strength was calculated. The typical relationship between stress and strain is plotted in Fig. 2. The ultimate tensile strength of the SLM Ti-6Al-4V alloy specimen was found as 813 MPa. The standard error value for tensile strength was found to be 13.2519 MPa and was observed to be less than 3% of the original value. The ultimate tensile strength of the conventional Ti-6Al-4V forged bar is 895 MPa, according to AMS 4928. The reduction of tensile strength of the SLM Ti-6Al-4V alloy specimen could be attributed to the microstructure refinement in the forged Ti-6Al-4V alloy. The fractured SLM Ti-6Al-4V alloy specimen was studied for fractography studies using a high-resolution scanning electron microscope. The fractured specimen fractography images are shown in Fig. 3a–c. The surface contour of the fractured specimen revealed the mode of a cup and cone fracture. Spherical dimples and micro-dimples that looked like a half micro-void were also observed. The secondary cracks, which are non-continuous and originate from primary cracks, were also observed. The presence of dimples was attributed to ductile fracture. Hence overall fracture mechanism would be concluded as the combination of both ductile and brittle fracture mechanisms.

3.4 Corrosion Characterization

3.4.1 Immersion Corrosion Test

The corrosion rate of the specimens was measured after an immersion period of 24 h (SLM01), 72 h (SLM02), 120 h (SLM03), and 168 h (SLM04). The average corrosion rate of the specimens in each batch was expressed in mm/year and is shown in Fig. 4. The corrosion rate steadily increased from 0 h and peaked after 24 h immersion. A maximum average corrosion rate of 9.07×10^{-4} mm/year was observed after 24 h of immersion. The increase in corrosion rate between 0 and 24 h of immersion was attributed to the exposure of new sites for corrosion. However, the formation of corrosion products was limited. Figure 5 shows the formation of limited corrosion products on the surface of the specimen after 24 h of immersion.

The corrosion rate dropped with a subsequent increase in immersion time up to 72 h. The lowest average corrosion rate of the specimens was 5.93×10^{-5} mm/year (after 72 h of immersion) for the batch SLM02. The formation of a layer of corrosion product on the specimen's surface after 72 h of immersion is evident in Fig. 6. A significant change was observed in the surface morphologies of the specimens after 24 h and 72 h of immersion. It was evident that a layer of corrosion product (or an interaction layer) was formed

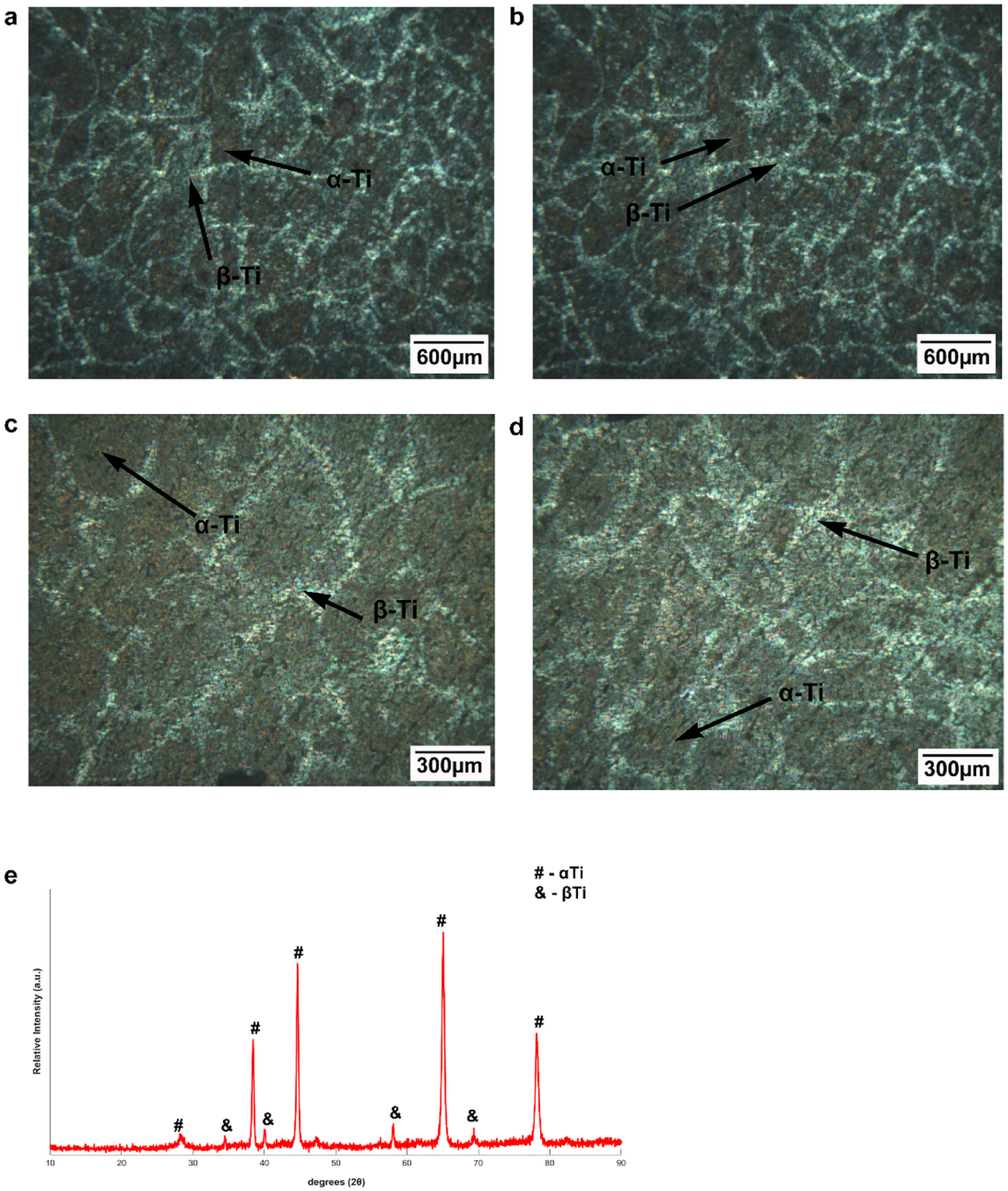

Fig. 1 **a–d** Microstructure of SLM Ti-6Al-4V alloy, **e** XRD analysis of the SLM Ti-4Al-6V alloy

between 24 and 72 h of immersion. The absence of new and active corrosion sites is attributed to a decrease in the corrosion rate of the specimens.

However, a marginal increase was observed in corrosion rate with a further increase in corrosion rate. The deviations in corrosion rate could be attributed to the dissolution of corrosion products (a partial fraction) into the solution paving the way for new corrosion sites and eventually increasing the corrosion rate. The average corrosion rate stood at 7.12×10^{-5} mm/year after 120 h of immersion. After 120 h, the corrosion rate was almost constant with minimal variations. The batch SLM04 exhibited an average corrosion rate of 7.51×10^{-5} mm/year (after 168 h), which was almost similar to the SLM03 specimen at 120 h. The limited availability of new corrosion sites could have resulted in a constant corrosion rate.

The corrosion rate of SLM Ti-6Al-4V in simulated body fluids was lesser than in other metal alloys. Titanium forms

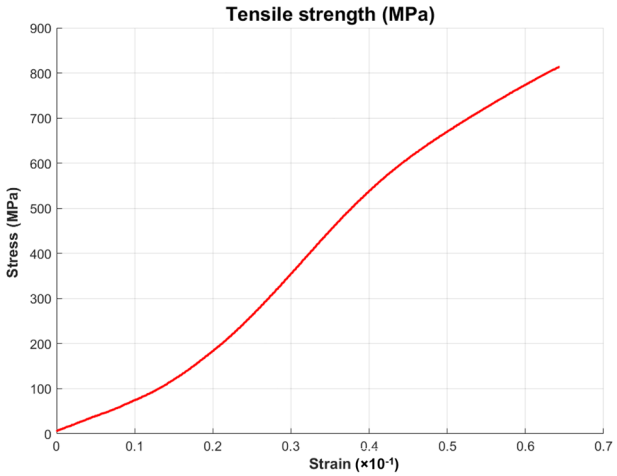

Fig. 2 Typical Stress–Strain Plot of the SLM Ti-4Al-6V alloy

a firm and adherent protective oxide layer (TiO, TiO_2, and Ti_2O_3) upon exposure to the air or moist environment. Hence, titanium has good corrosion resistance (Pilling–Bedworth ratio). However, DPBS contains aggressive ions such as Ca^{2+}, Mg^{2+}, Na^+, K^+, Cl^-, HPO_4^{2-}, and $H_2PO_4^-$. Though titanium has good resistance to those ions at room temperature and high temperature, the presence of more concentrations of Ca^{2+} and Mg^{2+} may induce localized corrosion on the titanium surface [41]. Most of the corrosion reactions in Ti-6Al-4V alloy are caused by the selective reaction of aluminum to DPBS. As aluminum loses as oxide layer (Al_2O_3) film on exposure to chlorides, it is highly corrosive to solutions of metal chlorides such as $CaCl_2$, $MgCl_2$, NaCl, and KCl. Aluminum is also slowly attacked by phosphates of Na and K. However, aluminum has limited interaction with disodium phosphates [42]. The vanadium present in the Ti-6Al-4V alloy is almost inert and does not react with oxides, chlorides, and phosphates. Vanadium forms a protective oxide layer of V_2O_5, which protects the Ti-6Al-4V alloy from corrosion. The presence of vanadium increased the corrosion resistance of the Ti-6Al-4V alloy in chloride-rich solutions. Vanadium addition in Ti-6Al-4V alloy also excludes the pitting corrosion in chlorine-rich solutions [43].

3.4.2 Surface Morphology and Elemental Composition Analysis

The surface morphology images of the SLM01, SLM02, SLM03, and SLM04 specimens were observed under the high-resolution scanning electron microscope. The typical surface morphology of the specimens in batch SLM01 is shown in Fig. 5. A magnified view showed the existence of the corrosion product as a flower-like structure formed by stacking corrosion products during the corrosion test.

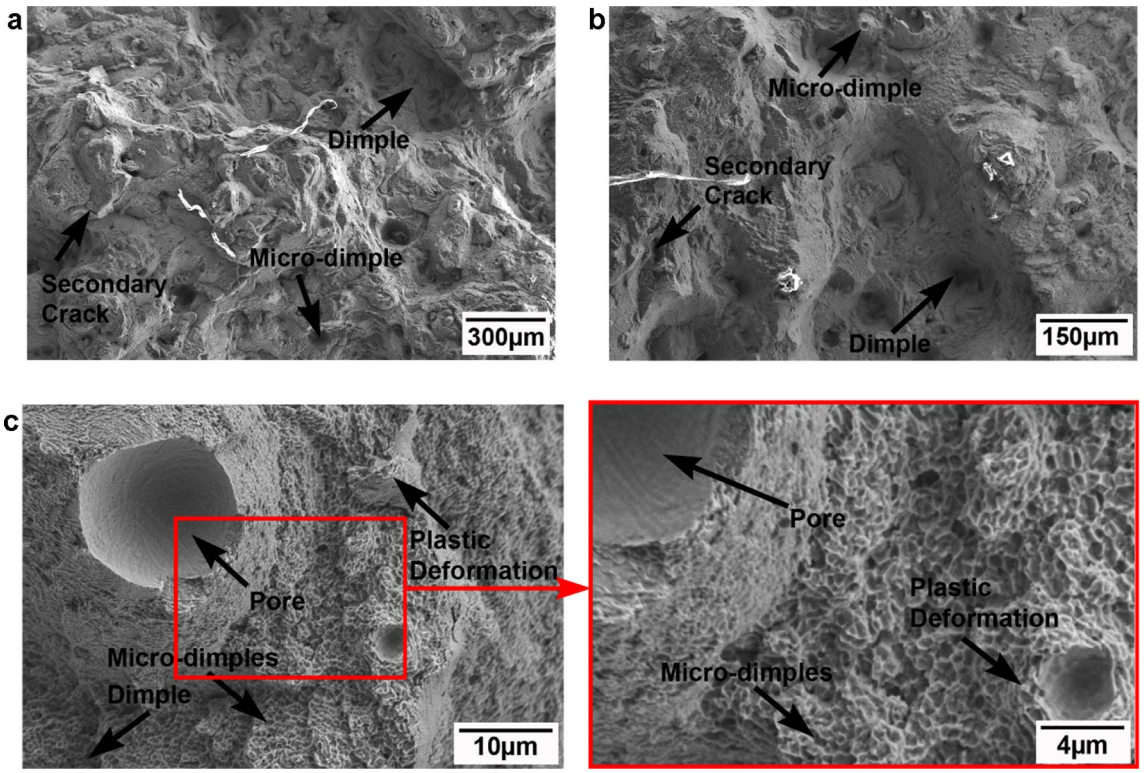

Fig. 3 **a–c** Fractography of SLM Ti-4Al-6V alloy specimen

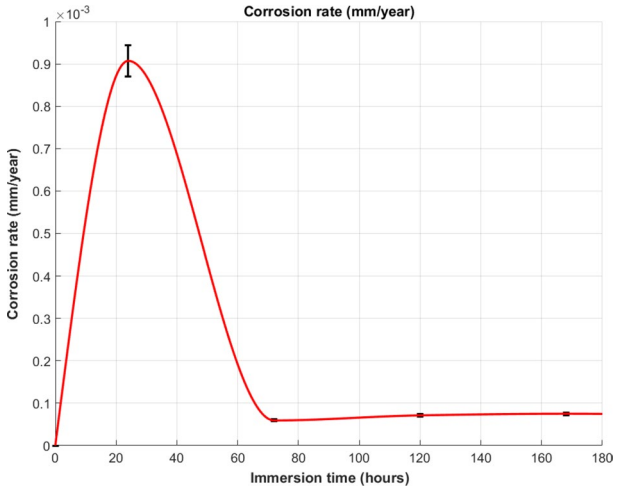

Fig. 4 Line graph of immersion corrosion rate of the specimen SLM Ti-6Al-4V

Also, cracks and pits were identified in the corrosion flower shown in Fig. 5.

The typical surface morphology of the specimens in batch SLM02 is shown in Fig. 6. The SLM02 specimen had numerous pits and some cracks on its surface. The corrosion product that exhibited crack and the delamination-like feature is magnified and shown in Fig. 6. Another typical surface morphology of the specimens in batch SLM02 is shown in Fig. 7a–c. A delaminated region and certain corrosion products are observed in Fig. 7a. The surface delaminated as the inherent oxide layer was damaged or the corrosion product dissolved into the solution. Figure 7b shows the presence of numerous pits and corrosion products over the surface. The cloud-like corrosion products hinted at the formation of porous hydroxyapatite layers.

The typical surface morphology of the specimens in batch SLM03 is shown in Fig. 8a, b. Few corrosion products scattered like grains and a delaminated region are observed in Fig. 8a. An enlarged view of a micro-pit is shown in Fig. 8b. The flower-like clusters on the surface of the specimens in batch SLM03 are shown in Fig. 9. The morphology of the corrosion products was similar to the observations of Vignesh et al. [44, 45]. This gives a clue to the possibility of the formation of hydroxyapatite.

The typical surface morphology of the specimens in batch SLM04 is shown in Fig. 10a–c. Figure 10a shows cracks with a crack tip on the corroded surface. A broad surface crack and sub-surface cracks were also observed, as shown excludes the pitting corrosion in chlorine-layers of corrosion products were observed in the specimen, as seen in Fig. 10c. Figure 11 confirms the presence of numerous cracks,

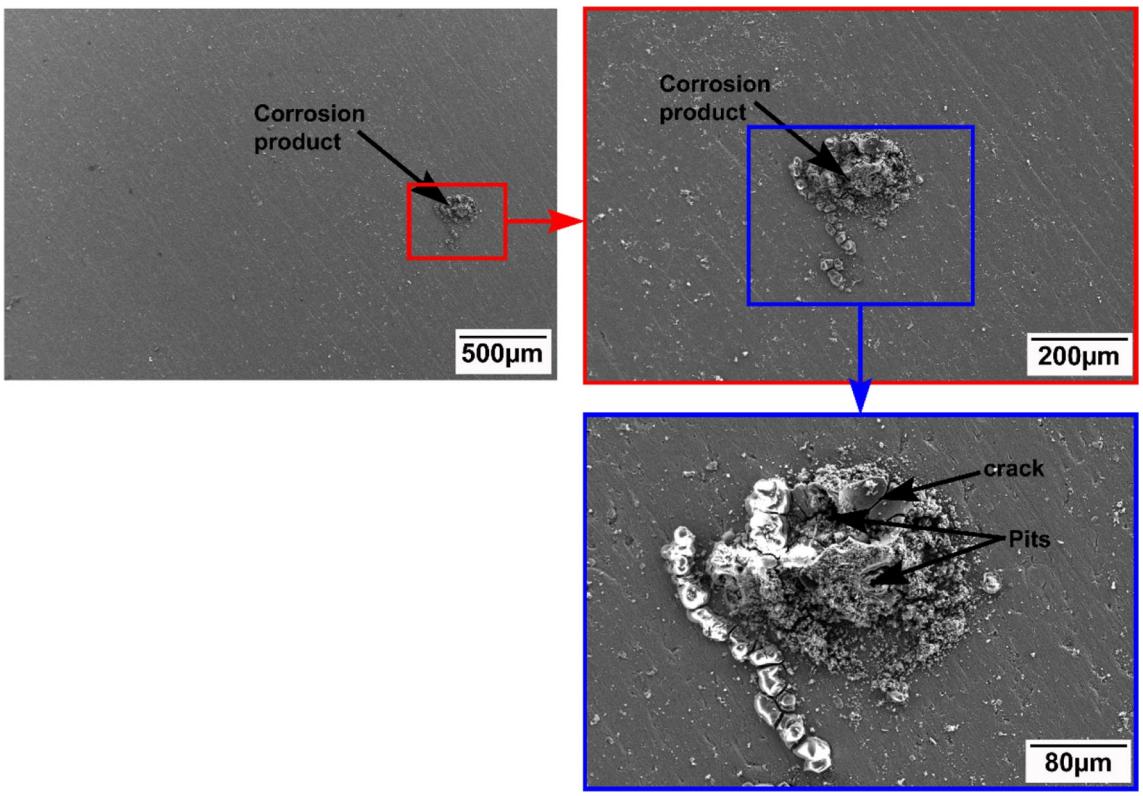

Fig. 5 Surface morphology of SLM01 specimen after immersion corrosion test for 24 h

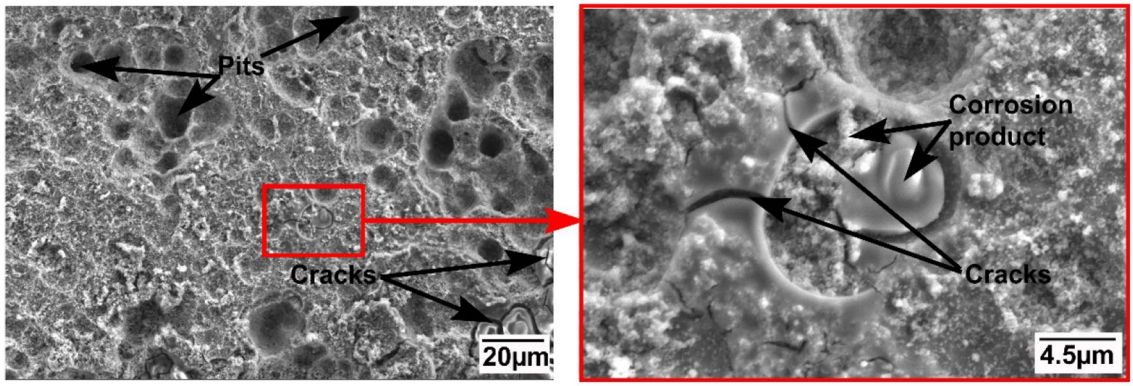

Fig. 6 Surface morphology of SLM02 specimen after immersion corrosion test for 48 h

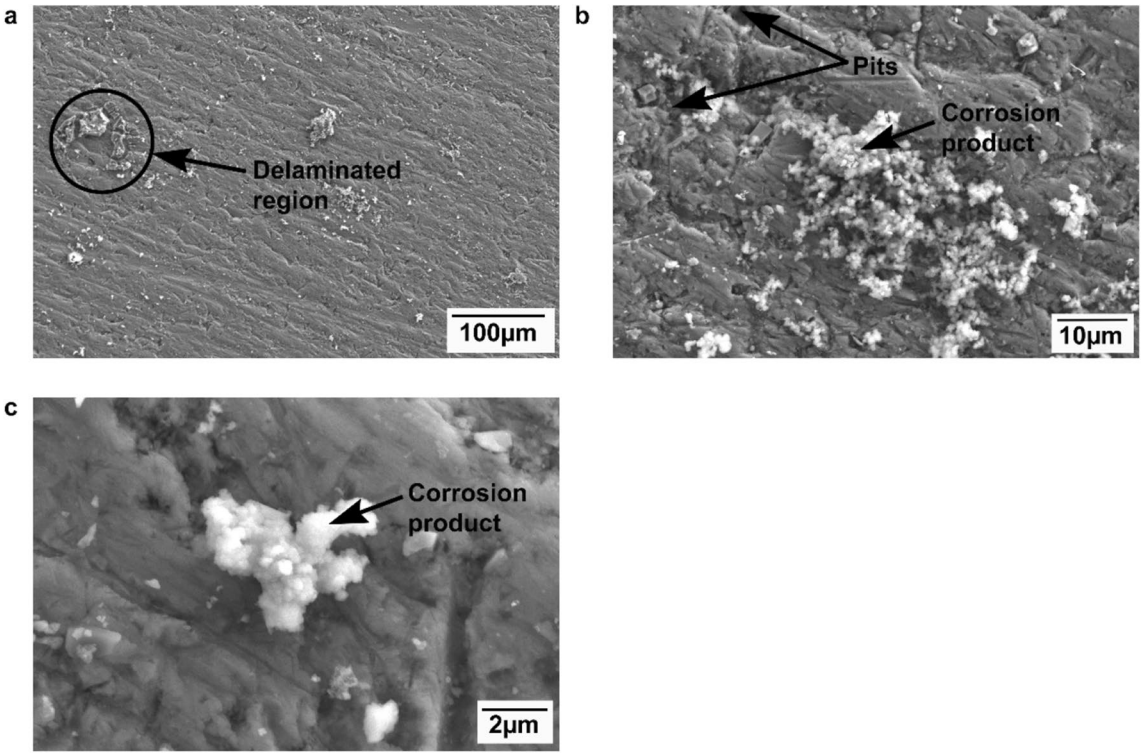

Fig. 7 **a–c** Surface morphology of SLM02 specimen after immersion corrosion test for 48 h

sub-surface cracks, and corrosion products on the surface. The inset in Fig. 11 shows the morphology of the cracked surface, indicating the surface and sub-surface cracks.

The elemental map of the corroded specimen from the batch SLM01 is shown in Fig. 12a–c. The mapping area of the corroded region is shown in Fig. 12a. The consolidated elemental map is shown in Fig. 12b. The individual elemental map is shown in Fig. 12c. The elemental map confirmed the presence of elements aluminum (Al), calcium (Ca), sodium (Na), oxygen (O), phosphorous (P), chlorine (Cl), magnesium (Mg), potassium (K), titanium (Ti), and vanadium (V). The corrosion product was primarily made of Al, Ca, Na, P, O, Cl elements and a few other trace elements that include Mg, Ti, K, and V. The presence of O, P, and Ca in the same region indicated the presence of calcium hydroxyapatite in the SLM01 specimen. The typical EDS spectra of the specimen in batch SLM01 supplemented the elemental map, as shown in Fig. 13a, b. The elemental concentration was as follows: Al (82.4 wt.%), O (6.4 wt.%), Cl (2.8 wt.%), Ca (2.8 wt.%), P (2.7 wt.%), Na (2.1 wt.%) and negligible quantity of Mg, V, K, and Ti. A majority of Al has been involved in the corrosion. The formed

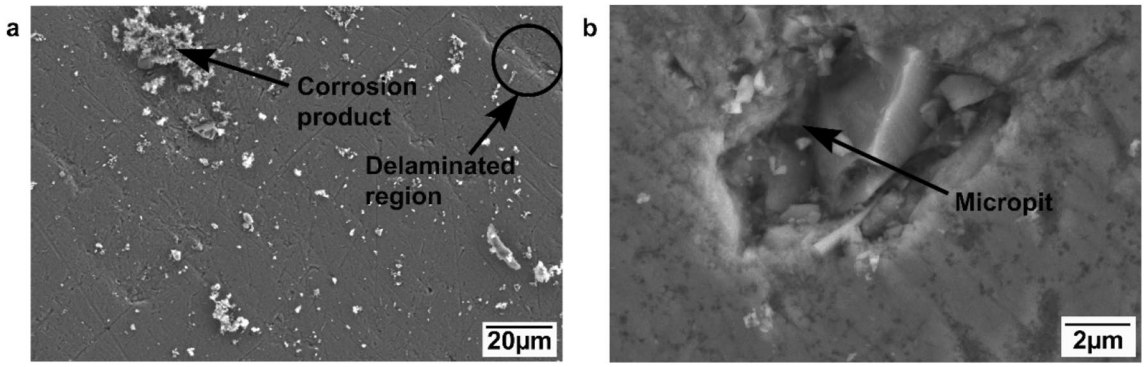

Fig. 8 **a–b** Surface morphology of SLM03 specimen after immersion corrosion test for 72 h

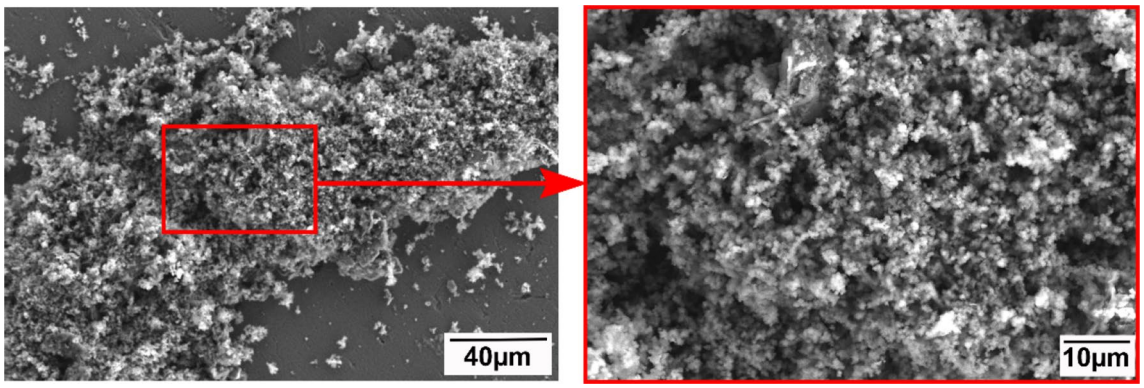

Fig. 9 Surface morphology of SLM03 specimen after immersion corrosion test for 72 h

corrosion products were aluminum oxide (Al_2O_3), calcium oxide (CaO), aluminum chloride ($AlCl_3$), calcium chloride ($CaCl_2$), sodium chloride (NaCl), and possible phosphates like calcium and magnesium phosphates. There may also be the formation of a few products like titanium oxide (TiO_2), vanadium chloride (V_2O_5), magnesium oxide (MgO), potassium chloride (KCl), magnesium chloride ($MgCl_2$), titanium chloride ($TiCl_4$), and vanadium chloride (VCl_3).

Figure 14a–c shows the elemental map images from the chosen region 1 of a typical specimen in batch SLM02. An oval gray patch of corrosion product was analyzed, and the results are shown in Fig. 14a. The consolidated and individual elemental maps are shown in Fig. 14b, c, respectively. The presence of elements Al, Ca, Na, O, P, Cl, Mg, K, Ti, and V was confirmed through the elemental map. The elemental map suggested that the significant elements in the corrosion product were Al, Na, P, O, and minor elements were Cl, Ca, Mg, Ti, K, and V. Hence, the corrosion product was more likely to be formed of Al, Na, P, O elements. The EDS spectra of the specimen are shown in Fig. 15a, b. The elemental composition in the specified spot was determined as follows: Al (75.9 wt.%), O (21.4 wt.%), P (0.9 wt.%), Na (0.8 wt.%), and negligible quantity of Cl, Ca, Mg, V, K, and Ti. The presence of more quantity of O indicates the formation of more oxide layers in the chosen region 1. The possible oxide corrosion products may be Al_2O_3, CaO, TiO_2, V_2O_5, MgO, and possible phosphates like calcium and magnesium phosphates. There may also be the formation of a few products like KCl, $AlCl_3$, $CaCl_2$, NaCl, $MgCl_2$, $TiCl_4$, and VCl_3.

A cloud-like corrosion product was also observed in the specimen (region 2), as shown in Fig. 16a. Figure 16b shows the consolidated elemental map, and Fig. 16c shows the individual elemental map. The elemental map demonstrated that the corroded region 2 consisted of Al, Ca, Na, P, O, and Cl elements in more fractions than Mg, Ti, K, and V elements. Most corrosion products were likely Al, Ca, Na, P, O, and Cl elements. The EDS spectra, as shown in Fig. 17a, b, confirmed the composition as follows: Al (86.5 wt.%), O (10.4 wt.%), P (1.5 wt.%), Ca (0.8 wt.%), Mg (0.4 wt.%), and negligible quantity of Cl, V, K and Ti in region 2. The presence of more O indicates the formation of more oxide layers in region 2 of the specimen. As observed, most of the corrosion activity has involved Al rather than other elements (Ti and V) of the base material. The possible oxide corrosion products may be Al_2O_3, CaO, TiO_2, V_2O_5, MgO,

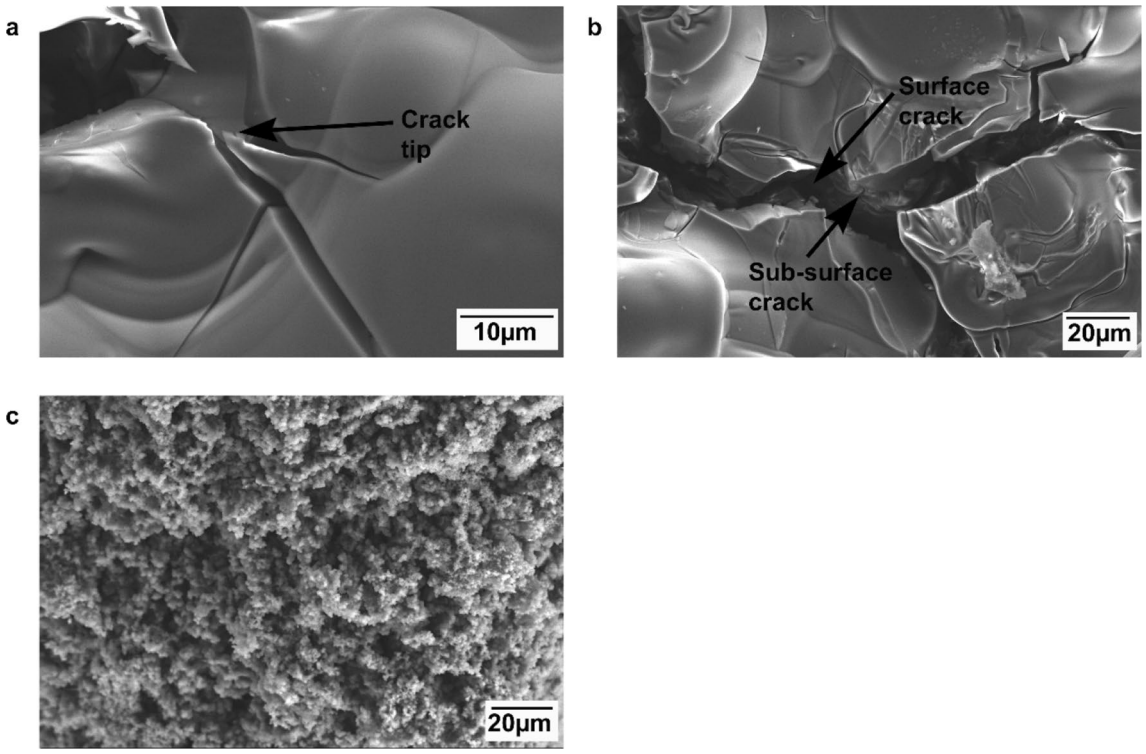

Fig. 10 **a–c** Surface morphology of SLM04 specimen after immersion corrosion test for 96 h

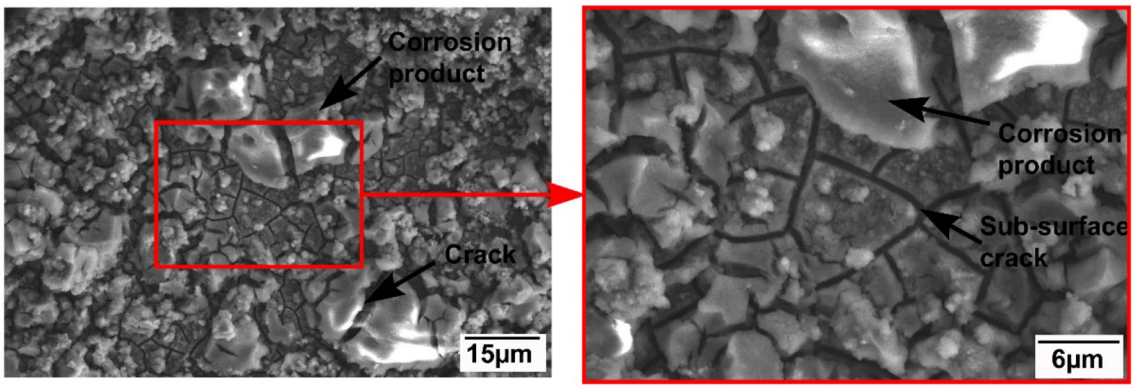

Fig. 11 Surface morphology of SLM04 specimen after immersion corrosion test for 96 h

and possible phosphates like calcium and magnesium phosphates. There may also be the formation of a few products like KCl, $MgCl_2$, $AlCl_3$, $CaCl_2$, NaCl, and $TiCl_4$.

3.4.3 Corrosion Mechanism

The presence of stable oxides of Ti and V on the surface restricts the corrosion in the SLM Ti-6Al-4V alloy. The stability of Ti and V oxide restrains from being removed or entirely dissolved in chlorides and phosphate-rich Dulbecco's phosphate-buffered solution that mimics the human biological environment. However, corrosion was observed in SLM Ti-6Al-4V alloy along with the formation of corrosion products. Al is one of the prime factors that initiated corrosion. The presence of Al in the SLM Ti-6Al-4V alloy forms an Al_2O_3 layer, as shown in Eqs. (4–8) [46].

Al during the period of immersion dissociated into Al^{3+} ions. The presence of dissolved oxygen leads to the formation of hydroxide ions. The formation of intermediate compound aluminum hydroxide ($Al(OH)_3$) expanded the specimen surface. $Al(OH)_3$ has limited solubility in water and is practically insoluble (solubility product, $K = 3 \times 10^{-34}$). The cumulative

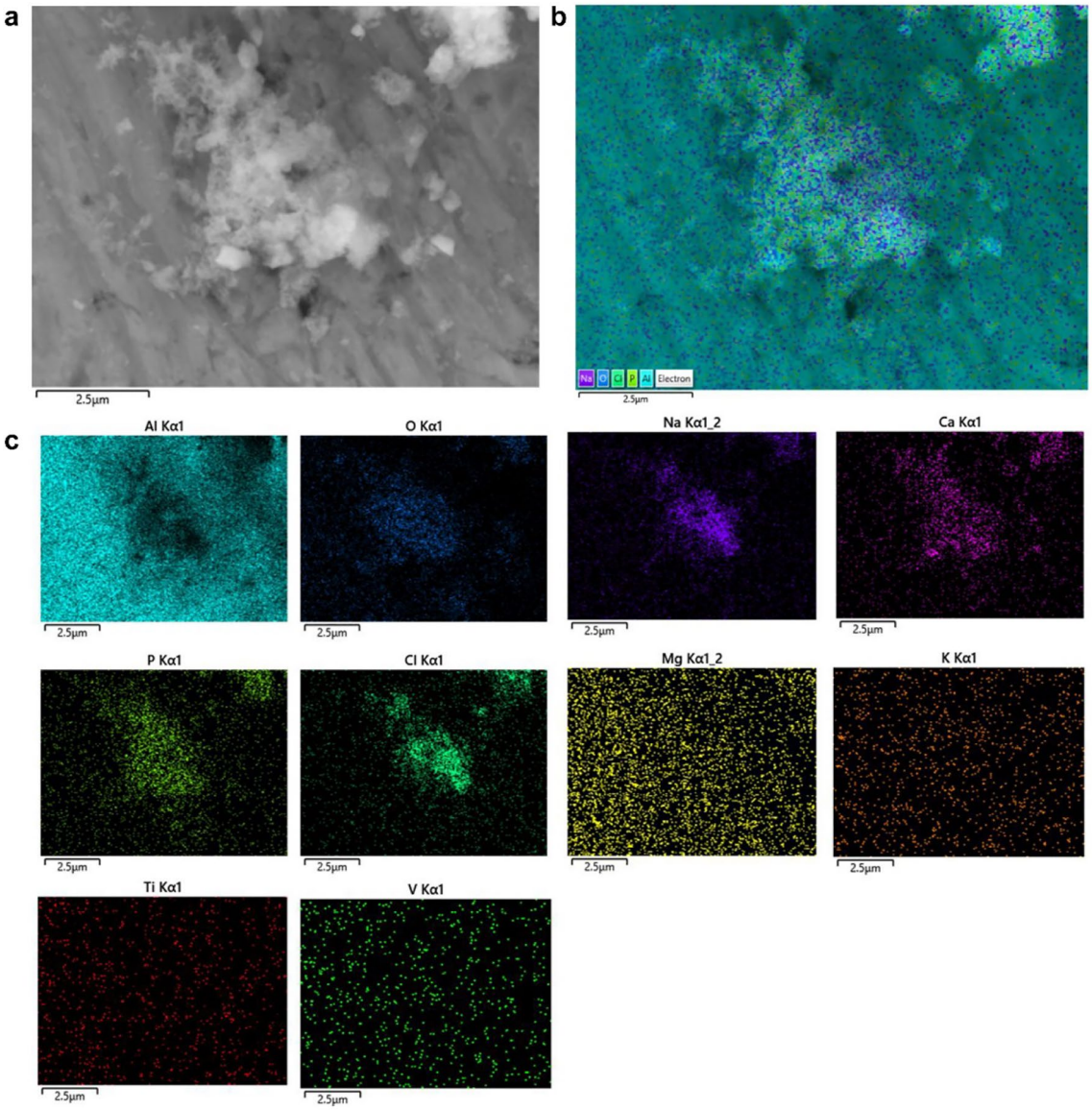

Fig. 12 **a–c** Elemental map of SLM01 specimen after immersion corrosion test for 24 h

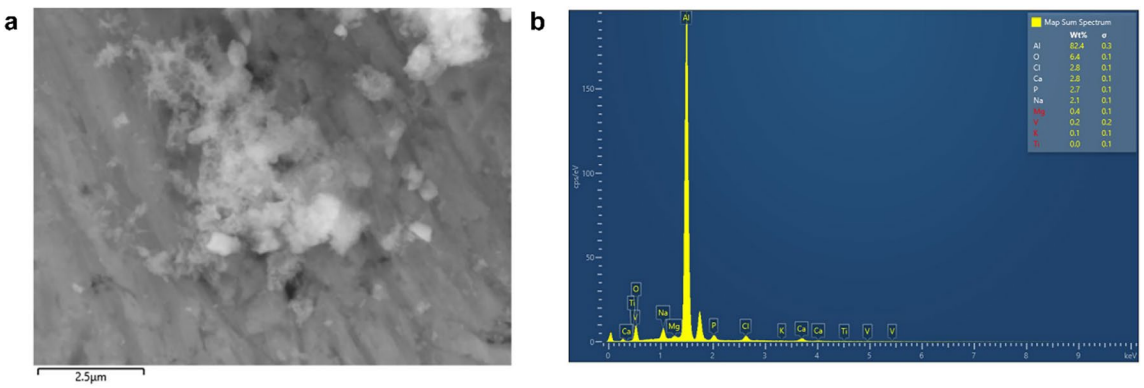

Fig. 13 **a**, **b)** Elemental composition of SLM01 specimen after immersion corrosion test for 24 h

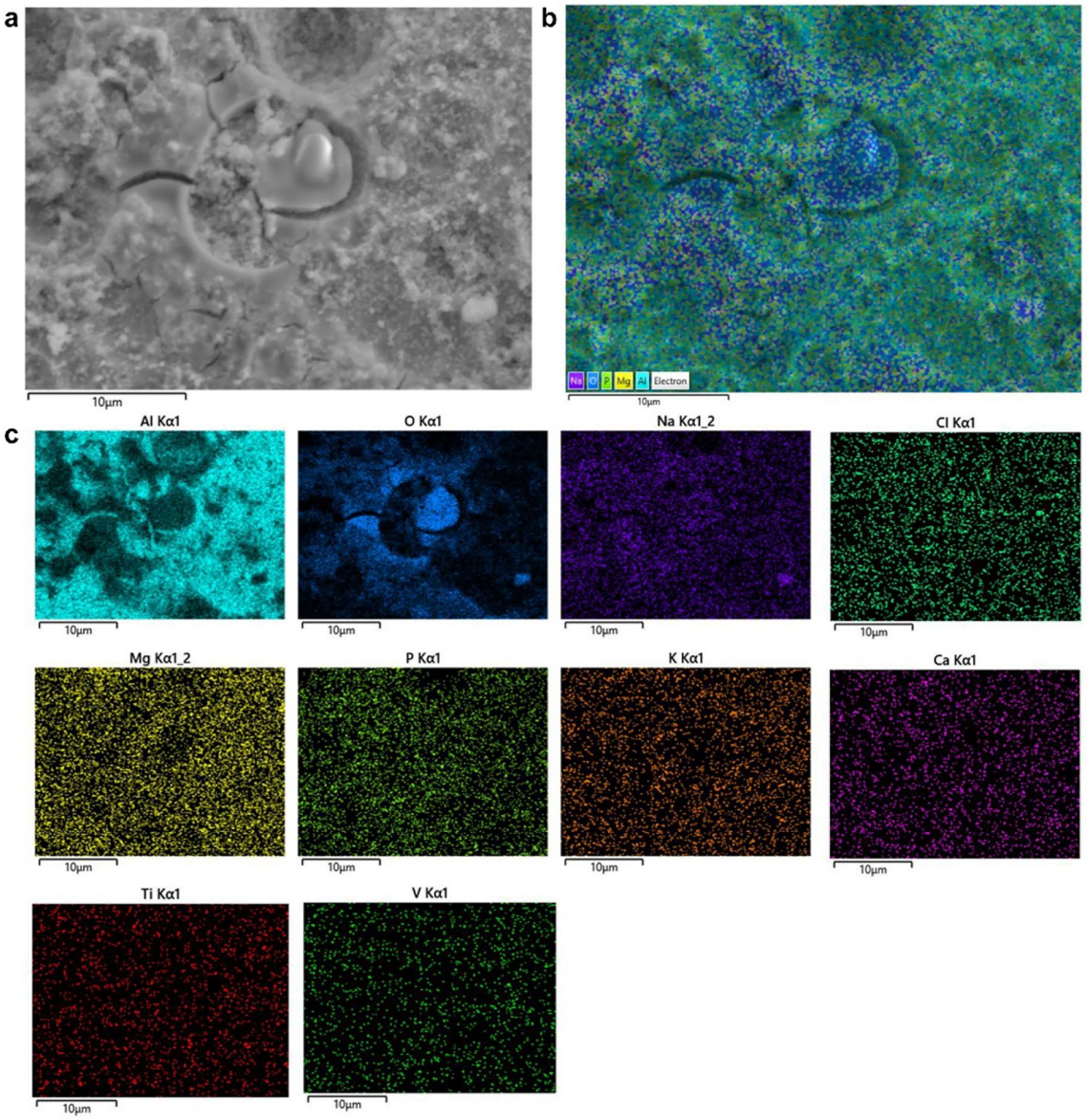

Fig. 14 **a–c** Elemental map of SLM02 specimen after immersion corrosion test for 48 h

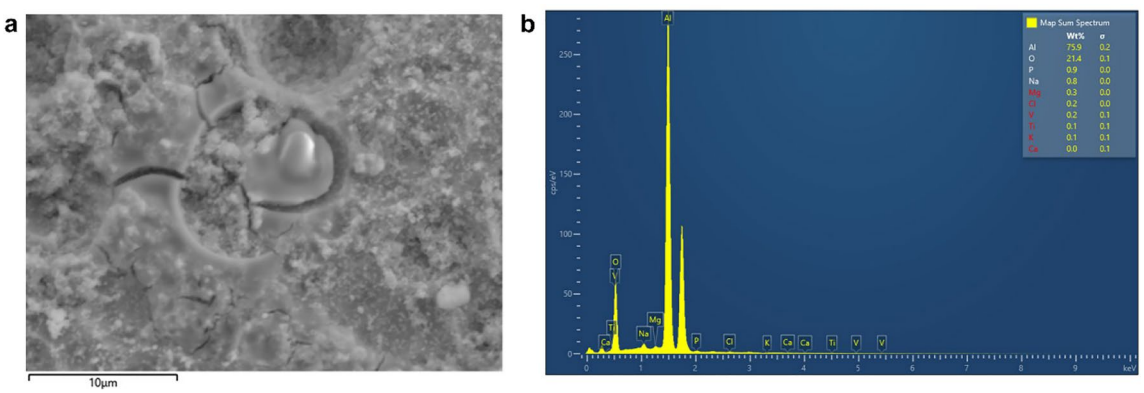

Fig. 15 **a**, **b** Elemental composition SLM02 specimen after immersion corrosion test for 48 h

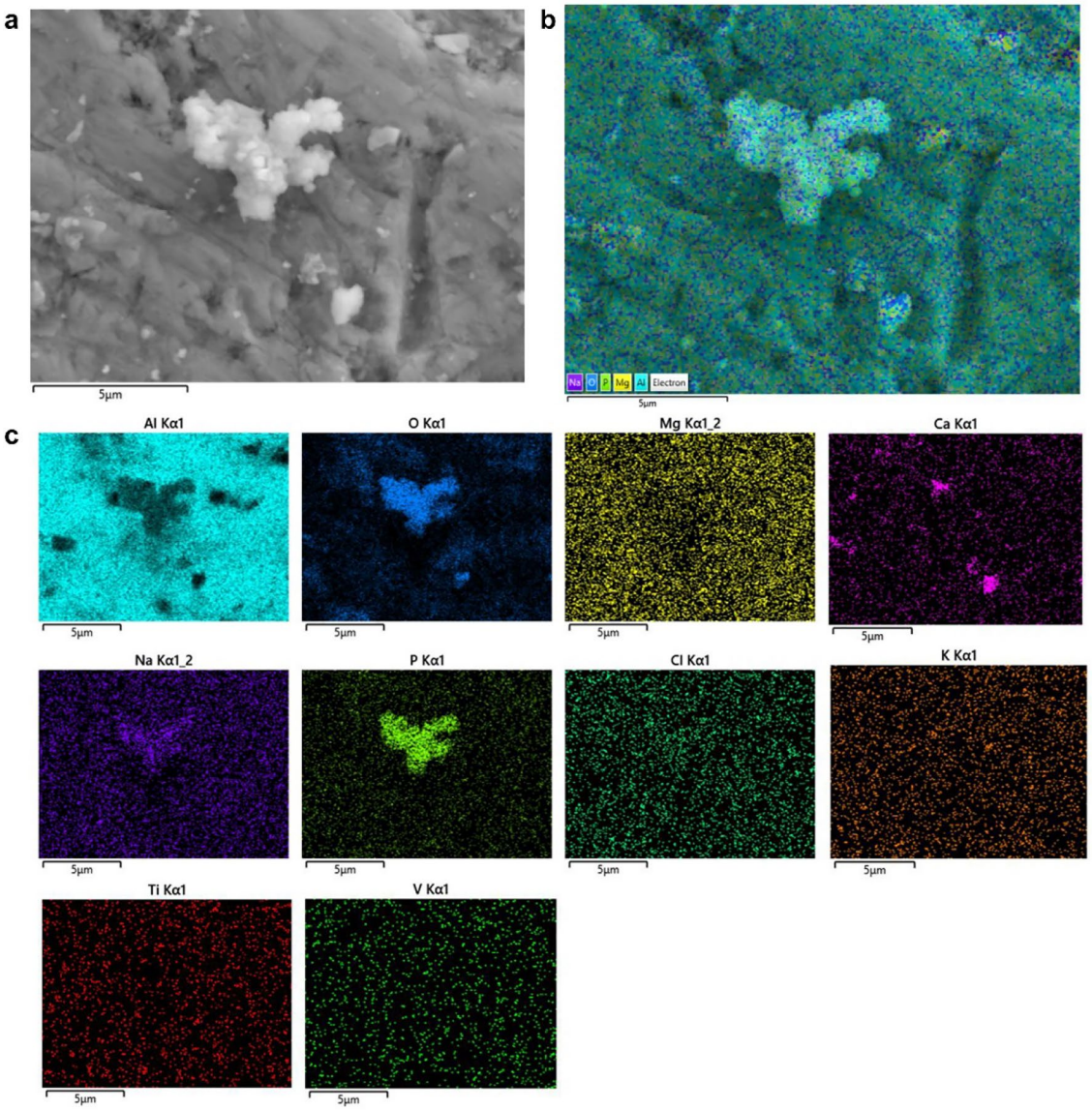

Fig. 16 **a–c** Elemental map of SLM02 specimen after immersion corrosion test for 48 h

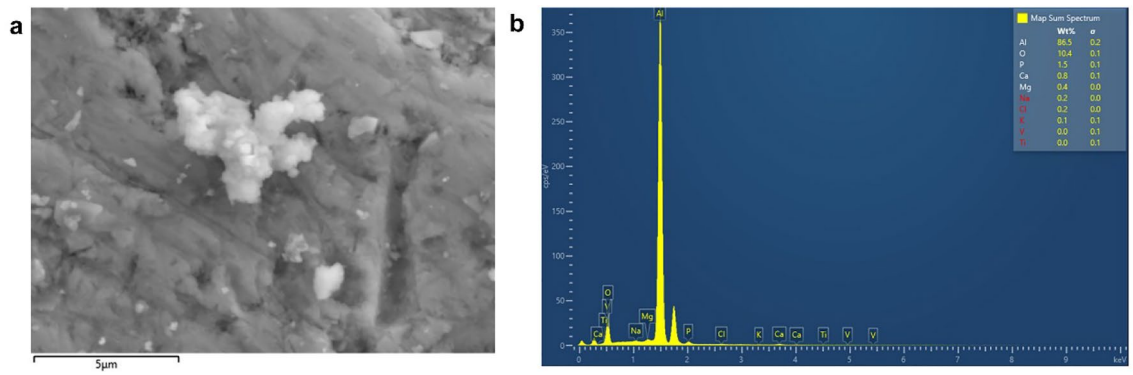

Fig. 17 **a**, **b** Elemental composition of SLM02 specimen after immersion corrosion test for 48 h

formation of $Al(OH)_3$ aided the surface crack formation and propagation. The oxide layer formed by Al is unstable to the chlorides and phosphates present in the solution. The Al reacts with chlorides to form aluminum chloride ($AlCl_3$).

$$Al \rightarrow Al^{3+} + 3e^- \tag{4}$$

$$2H_2O + 4e^- + O_2 \rightarrow 4OH^- \tag{5}$$

$$Al^{3+} + 3OH^- \rightarrow Al(OH)_3 + 3e^- \tag{6}$$

Equation 7 shows the reaction of Al with the chloride ions (Cl^-). However, highly reactive Cl^- ions having a smaller radius penetrates $Al(OH)_3$. The $Al(OH)_3$ readily reacted with Cl^- forming $AlCl_3$. $AlCl_3$ has a solubility of 45.8 g in 100 ml at 20 °C. Hence, the $AlCl_3$ formed is solvable in water. This caused delaminated regions on the surface that acted as newly exposed sites for corrosion.

$$Al(OH)_3 + 3Cl^- \rightarrow AlCl_3 + 3(OH)^- \tag{7}$$

$$2Al + 3H_2O \rightarrow Al_2O_3 + 6H^+ + 6e^- \tag{8}$$

The corrosion products might also have chlorides of Ti and V. The presence of more concentrations of Ca^+ and Mg^+ ions in the solution may induce a reaction of Ti and V with the chloride ions [41]. The oxide film in SLM Ti-6Al-4V alloy mainly consists of TiO_2. However, the open literature also reported the possibility of forming TiO, Ti_2O_3, and Ti_3O_5 [47]. Even though Ti_2O_3 and Ti_3O_5 are more stable than TiO_2 according to thermodynamics theory, the oxide layer is mostly TiO_2 because of the influence of temperature and partial pressure of oxygen.

The reaction of Ti and O_2 forms Ti_3O_5, Ti_2O_3, TiO_2, and TiO, respectively, as given in Eqs. (9–12). TiO_2 is more likely formed by the further oxidation of low valance oxides like TiO, Ti_2O_3, and Ti_3O_5 than the direct oxidation of the titanium. Eqs. (13–15) show the oxidation of low valance titanium oxides to TiO_2. At higher temperatures, the low valance oxides are more likely present on the surface than TiO_2 [47]. As the TiO_2 is highly stable, Ti^{4+} ions are not easily formed from TiO_2 during the corrosion. In the event of dissociation of TiO_2, Ti^{4+} ions react with chloride ions to form $TiCl_4$, as given in Eq. (16). However, a limited fraction of $TiCl_4$ might have formed because of the high stability of TiO_2.

$$3Ti + \frac{5}{2}O_2 \rightarrow Ti_3O_5 \tag{9}$$

$$2Ti + \frac{3}{2}O_2 \rightarrow Ti_2O_3 \tag{10}$$

$$Ti + O_2 \rightarrow TiO_2 \tag{11}$$

$$Ti + \frac{1}{2}O_2 \rightarrow TiO \tag{12}$$

$$TiO + \frac{1}{2}O_2 \rightarrow TiO_2 \tag{13}$$

$$\frac{1}{2}Ti_2O_3 + \frac{1}{4}O_2 \rightarrow TiO_2 \tag{14}$$

$$\frac{1}{3}Ti_3O_5 + \frac{1}{6}O_2 \rightarrow TiO_2 \tag{15}$$

$$Ti^{4+} + Cl^- \rightarrow TiCl_4 \tag{16}$$

Vanadium oxidizes to VO_2 and V_2O_5. The vanadium reacts with oxygen to form a significant content of V_2O_5 as per Eq. (17) [47].

$$2V + \frac{5}{2}O_2 \rightarrow V_2O_5 \tag{17}$$

The overlapping of individual elemental maps of Ca, O, P, and some Mg in the same regions of the corrosion product indicated the presence of calcium hydroxyapatite or calcium magnesium phosphates. Equation (18) and (19) shows the formation of calcium and magnesium phosphate [44]. Equation (20) shows the formation of calcium hydroxyapatite ($Ca_{10}(PO_4)_6(OH)_2$) [48]. Calcium hydroxyapatite promotes bone growth and enables effective bone–implant integration [35, 45, 49, 50]. Calcium hydroxyapatite formation decreases the rate of corrosion. Some forms of calcium magnesium apatite were also observed in the mapping images. Equation (21) shows the formation of calcium magnesium apatite [51].

$$\left(PO_4^{3-}\right) + Ca^{2+} + O^{2-} + 3H^+ \rightarrow CaH(PO_4) \tag{18}$$

$$\left(PO_4^{3-}\right) + Mg^{2+} + O^{2-} + 3H^+ \rightarrow MgH(PO_4) \tag{19}$$

$$6\left(PO_4^{3-}\right) + 10Ca^{2+} + 2OH^- \rightarrow Ca_{10}(PO_4)_6(OH)_2 \tag{20}$$

$$\left(PO_4^{3-}\right) + Mg^{2+} + Ca^{2+} + OH^- \rightarrow Ca_{10-x}Mg_x(PO_4)_6(OH)_2 \tag{21}$$

3.5 Electrochemical corrosion

The electrochemical corrosion test was carried out to evaluate the anodic and cathodic performance of SLM Ti-6Al-4V alloy. Figure 18 shows the open circuit potential (OCP) and potentiodynamic polarization plot of the SLM Ti-6Al-4V alloy in the DPB solution. The OCP of SLM Ti-6Al-4V alloy was observed to be − 0.65 V. The corrosion potential

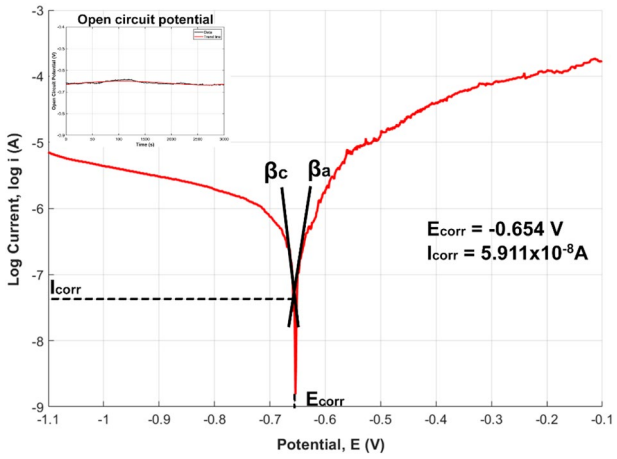

Fig. 18 Tafel plot and open circuit potential plot

at which the rate of cathodic reaction and the rate of anodic dissolution complement each other is the corrosion potential (E_{corr}). E_{corr} was determined from the potentiodynamic polarization plot. The curve of cathodic polarization (E lesser than E_{corr}) corresponds to the stage of cathodic reaction. In contrast, the anodic polarization curve (E greater than E_{corr}) is the stage of anodic dissolution. The E_{corr} value obtained from the potentiodynamic polarization graph was − 0.654V.

The presence of an irregular curve in the anodic curve shows the existence of pitting corrosion during potentiodynamic polarization. The region between $E_{corr} \pm 20$ mV is termed the Tafel region. Tangent was drawn to the cathodic polarization curve and the anodic polarization curve that meets in the Tafel region. The point where both tangents intersect corresponds to corrosion current I_{corr}. The I_{corr} value obtained from the potentiodynamic polarization graph was 5.91×10^{-8} A. The chloride ions react with titanium only after the dissolution of the TiO_2 oxide layer in the SLM Ti-6Al-4V alloy. Once the oxide layer is removed, Ti^{4+} ions are formed. These Ti^{4+} ions react with the Cl^- ions in DBF solution and form titanium tetrachloride ($TiCl_4$). The formation of $TiCl_4$ is shown in Eq. (22).

$$Ti^{4+} + Cl^- \rightarrow TiCl_4 \tag{22}$$

Due to the high polarity of water (Polarity index = 1), the $TiCl_4$ reacts with water to form TiO_2. Equation (23) shows the formation of TiO_2 from $TiCl_4$.

$$TiCl_4 + 2H_2O \rightarrow TiO_2 + 4H^+ + 4Cl^- \tag{23}$$

TiO_2 did not react with other compounds in the electrolyte solution, as it had a strong bond to titanium. Thus, TiO_2 adhered to the surface of the SLM Ti–6Al–4V electrode to form a stable oxide layer [52]. Other than titanium, aluminum in the alloy also reacts with the electrolyte. Aluminum forms Al^{3+} ions during the anodic reaction. The Al^{3+} ions undergo hydrolysis with the water present in the electrolyte to form aluminum hydroxide. Equations (24) and (25) show the aluminum's hydrolysis reaction.

$$Al^{3+} + H_2O \rightarrow Al(OH)^{2+} + 2H^+ \tag{24}$$

$$Al^{3+} + 2H_2O \rightarrow Al(OH)_2^+ + 2H^+ \tag{25}$$

There is a high concentration of Cl^- ions present in the electrolyte. The aluminum hydroxide reacts with the Cl^- ions, water, and Na^+ ions to form aluminum chloride ($AlCl_3$). Equations (26) and (27) show the reaction of aluminum hydroxide with the Cl^- ions. Eq. (28) shows the reaction of Na^+ and Cl^- ions present in the electrolyte with the $Al(OH)_2Cl$ formed Eq. (27). The formation of $AlCl_3$ is an infinitesimal quantity as the aluminum is in a smaller amount in the Ti-6Al-4V alloy [53].

$$Al(OH)^{2+} + Cl^- \rightarrow Al(OH)Cl^+ \tag{26}$$

$$Al(OH)Cl^+ + H_2O \rightarrow Al(OH)_2Cl + H^+ \tag{27}$$

$$2Al(OH)_2Cl + 4Na^+ + 4Cl^- \rightarrow 2AlCl_3 + 4NaOH. \tag{28}$$

4 Conclusion

Ti-6Al-4V alloy was successfully fabricated by selective laser melting technology. The microstructure, microhardness, tensile strength, and corrosion behavior of the fabricated specimen were determined. The key findings of the present investigation are as follows:

- The microstructure of SLM Ti-6Al-4V alloy consisted of α and β phases. The fabricated specimen exhibited a continuous networked structure of the β phase
- The SLM Ti-6Al-4V alloy had an average microhardness of 255 HV and ultimate tensile strength of 813 MPa. The fractography attested to the predominance of both ductile and brittle fracture mechanisms.
- The corrosion rate of the SLM Ti-6Al-4V alloy in simulated body fluid was 9×10^{-4} mm/year. The formation of calcium hydroxyapatite that mimics the human physiological bone material is evident from the analysis. Hence, the SLM Ti-6Al-4V alloy would have good biocompatibility during implantation.
- The present study gives scope for utilization of the SLM method for fabrication of Ti-6Al-4V, which has profound applications in the medical field.. Further, the properties of the material could be improved by heat treatment

methods and other processes like anodizing depending on the application.

Author contributions All authors contributed to the study's conception and design. All the authors performed material preparation, data collection, and analysis. The first draft of the manuscript was written by B G Yashwant Kumar and R Lokesh Kumar. All authors commented on previous versions of the manuscript. All authors read and approved the final manuscript.

Funding The authors and co-authors did not receive a specific grant from any funding agency in the public, commercial, or not-for-profit sectors to carry out the research.

Availability of data and material (data transparency) All data generated or analyzed during this study are included in this published article (and its supplementary information files).

Code availability Not Applicable.

Declarations

Conflict of interest The authors declare no conflict of interest or competing interests in the research work.

Ethics approval Not Applicable.

Consent to participate Not Applicable.

Consent for publication The author transfers to the concerned publisher the non-exclusive publication rights and the warrants that his/her contribution is original and that he/she has full power to make this grant. The author signs for and accepts responsibility for releasing this material on behalf of any and all co-authors. This transfer of publication rights covers the non-exclusive right to reproduce and distribute the article, including reprints, translations, photographic reproductions, microform, electronic form (offline, online) or any other reproductions of similar nature.

References

1. Rodri´guez D, et al (1999) Titanium levels in rats implanted with Ti6Al4V treated samples in the absence of wear. J Mater Sci Mater Med 10(12):847–851. https://doi.org/10.1023/A:1008912831051
2. de Viteri VS (2013) Titanium and titanium alloys as biomaterials. In: Gegner EFEJ (eds) Rijeka: IntechOpen
3. Vaira Vignesh R, Padmanaban R, Govindaraju M, Suganya Priyadharshini G (2019) Investigations on the corrosion behaviour and biocompatibility of magnesium alloy surface composites AZ91D-ZrO_2 fabricated by friction stir processing. Trans IMF 97(5):261–270. https://doi.org/10.1080/00202967.2019.1648005
4. Ramalingam VV, Ramasamy P, Kovukkal MD, Myilsamy G (2020) Research and development in magnesium alloys for industrial and biomedical applications: a review. Met Mater Int 26(4):409–430. https://doi.org/10.1007/s12540-019-00346-8
5. Bingjing Z, Hong W, Ning Q, Chao W, Min H (2016) Corrosion resistance characteristics of a Ti-6Al-4V alloy scaffold that is fabricated by electron beam melting and selective laser melting for implantation in vivo. Mater Sci Eng C. https://doi.org/10.1016/j.msec.2016.07.045
6. Veiga C, Davim JP, Loureiro AJR (2012) Properties and applications of titanium alloys: a brief review. Rev Adv Mater Sci 32(2):133–148
7. Avila JD, Bose S, Bandyopadhyay A (2018) Additive manufacturing of titanium and titanium alloys for biomedical applications. Titan Med Dent Appl. https://doi.org/10.1016/B978-0-12-812456-7.00015-9
8. Niinomi M (2008) Mechanical biocompatibilities of titanium alloys for biomedical applications. J Mech Behav Biomed Mater 1(1):30–42
9. Cimenoglu H, Gunyuz M, Kose GT, Baydogan M, Uğurlu F, Sener C (2011) Micro-arc oxidation of Ti6Al4V and Ti6Al7Nb alloys for biomedical applications. Mater Charact 62(3):304–311. https://doi.org/10.1016/j.matchar.2011.01.002
10. Murr LE et al (2009) Microstructure and mechanical behavior of Ti-6Al-4V produced by rapid-layer manufacturing, for biomedical applications. J Mech Behav Biomed Mater 2(1):20–32. https://doi.org/10.1016/j.jmbbm.2008.05.004
11. Zhou L, Yuan T, Tang J, He J, Li R (2019) Mechanical and corrosion behavior of titanium alloys additively manufactured by selective laser melting—a comparison between nearly β titanium, α titanium and $\alpha + \beta$ titanium. Opt Laser Technol 119:105625. https://doi.org/10.1016/j.optlastec.2019.105625
12. Almangour B (2018) Additive manufacturing of emerging materials. Addit Manuf Emerg Mater. https://doi.org/10.1007/978-3-319-91713-9
13. Yan Q et al (2020) Comparison study on microstructure and mechanical properties of Ti-6Al-4V alloys fabricated by powder-based selective-laser-melting and sintering methods. Mater Charact. https://doi.org/10.1016/j.matchar.2020.110358
14. Tamayo JA, Riascos M, Vargas CA, Baena LM (2021) Additive manufacturing of Ti6Al4V alloy via electron beam melting for the development of implants for the biomedical industry. Heliyon. https://doi.org/10.1016/j.heliyon.2021.e06892
15. Liu S, Shin YC (2019) Additive manufacturing of Ti6Al4V alloy: a review. Mater Des 164:107552. https://doi.org/10.1016/j.matdes.2018.107552
16. Soyama H, Sanders D (2019) Use of an abrasive water cavitating jet and peening process to improve the fatigue strength of titanium alloy 6al-4v manufactured by the electron beam powder bed melting (EBPB) additive manufacturing method. JOM 71(12):4311–4318. https://doi.org/10.1007/s11837-019-03673-8
17. Hao Y-L, Li S-J, Yang R (2016) Biomedical titanium alloys and their additive manufacturing. Rare Met 35(9):661–671. https://doi.org/10.1007/s12598-016-0793-5
18. Arias-González F et al (2018) Microstructure and crystallographic texture of pure titanium parts generated by laser additive manufacturing. Met Mater Int 24(1):231–239. https://doi.org/10.1007/s12540-017-7094-x
19. Bikas H, Stavropoulos P, Chryssolouris G (2016) Additive manufacturing methods and modelling approaches: a critical review. Int J Adv Manuf Technol 83(1):389–405. https://doi.org/10.1007/s00170-015-7576-2
20. Pal S et al (2020) Evolution of the metallurgical properties of Ti-6Al-4V, produced with different laser processing parameters, at constant energy density in Selective Laser Melting. Results Phys 17:103186. https://doi.org/10.1016/j.rinp.2020.103186
21. Beese AM, Carroll BE (2016) Review of mechanical properties of ti-6al-4v made by laser-based additive manufacturing using powder feedstock. JOM 68(3):724–734. https://doi.org/10.1007/s11837-015-1759-z

22. Xie Z, Dai Y, Ou X, Ni S, Song M (2020) Effects of selective laser melting build orientations on the microstructure and tensile performance of Ti-6Al-4V alloy. Mater Sci Eng A 776:139001. https://doi.org/10.1016/j.msea.2020.139001
23. Tuomi JT et al (2017) In vitro cytotoxicity and surface topography evaluation of additive manufacturing titanium implant materials. J Mater Sci Mater Med 28(3):53. https://doi.org/10.1007/s10856-017-5863-1
24. Sharma A, Oh MC, Kim J-T, Srivastava AK, Ahn B (2020) Investigation of electrochemical corrosion behavior of additive manufactured Ti-6Al-4V alloy for medical implants in different electrolytes. J Alloys Compd 830:154620. https://doi.org/10.1016/j.jallcom.2020.154620
25. Yang J, Yu H, Yin J, Gao M, Wang Z, Zeng X (2016) Formation and control of martensite in Ti-6Al-4V alloy produced by selective laser melting. Mater Des 108:308–318. https://doi.org/10.1016/j.matdes.2016.06.117
26. Pal S, Lojen G, Kokol V, Drstvensek I (2018) Evolution of metallurgical properties of Ti-6Al-4V alloy fabricated in different energy densities in the Selective Laser Melting technique. J Manuf Process 35:538–546. https://doi.org/10.1016/j.jmapro.2018.09.012
27. Chandramohan P, Bhero S, Obadele BA, Olubambi PA (2017) Laser additive manufactured Ti-6Al-4V alloy: tribology and corrosion studies. Int J Adv Manuf Technol 92(5):3051–3061. https://doi.org/10.1007/s00170-017-0410-2
28. Longhitano GA et al (2018) Heat treatments effects on functionalization and corrosion behavior of Ti-6Al-4V ELI alloy made by additive manufacturing. J Alloys Compd 765:961–968. https://doi.org/10.1016/j.jallcom.2018.06.319
29. Tsai M-T et al (2020) Heat-treatment effects on mechanical properties and microstructure evolution of Ti-6Al-4V alloy fabricated by laser powder bed fusion. J Alloys Compd 816:152615. https://doi.org/10.1016/j.jallcom.2019.152615
30. Kusano M et al (2020) Tensile properties prediction by multiple linear regression analysis for selective laser melted and post heat-treated Ti-6Al-4V with microstructural quantification. Mater Sci Eng A 787:139549. https://doi.org/10.1016/j.msea.2020.139549
31. Ettefagh AH, Zeng C, Guo S, Raush J (2019) Corrosion behavior of additively manufactured Ti-6Al-4V parts and the effect of post annealing. Addit Manuf 28:252–258. https://doi.org/10.1016/j.addma.2019.05.011
32. Mierzejewska ŻA, Hudák R, Sidun J (2019) Mechanical properties and microstructure of DMLS Ti6Al4V alloy dedicated to biomedical applications. Mater (Basel, Switzerland) 12(1):176. https://doi.org/10.3390/ma12010176
33. Shunmugavel M, Polishetty A, Goldberg M, Singh R, Littlefair G (2017) A comparative study of mechanical properties and machinability of wrought and additive manufactured (selective laser melting) titanium alloy—Ti-6Al-4V. Rapid Prototyp J 23(6):1051–1056. https://doi.org/10.1108/RPJ-08-2015-0105
34. Sun J, Zhu X, Qiu L, Wang F, Yang Y, Guo L (2019) The microstructure transformation of selective laser melted Ti-6Al-4V alloy. Mater Today Commun 19:277–285. https://doi.org/10.1016/j.mtcomm.2019.02.006
35. Vignesh RV, Padmanaban R, Govindaraju M (2019) Study on the corrosion and wear characteristics of magnesium alloy AZ91D in simulated body fluids. Bull Mater Sci 43(1):8. https://doi.org/10.1007/s12034-019-1973-3
36. Tahmasebifar A, Kayhan SM, Evis Z, Koç M, Tezcaner A, Çinici H (2016) AC SC. J Alloys Compd. https://doi.org/10.1016/j.jallcom.2016.05.256
37. Bharathi BM, Vignesh RV, Padmanaban R, Govindaraju M (2020) Effect of friction stir processing and heat treatment on the corrosion properties of AZ31 alloy. Aust J Mech Eng. https://doi.org/10.1080/14484846.2020.1815999
38. Fontana MG (1986) Corrosion engineering. McGraw-Hill, New York
39. Shi X, Zeng W, Sun Y, Han Y, Zhao Y, Guo P (2015) Microstructure-tensile properties correlation for the Ti-6Al-4V titanium alloy. J Mater Eng Perform 24(4):1754–1762. https://doi.org/10.1007/s11665-015-1437-x
40. Poondla N, Srivatsan TS, Patnaik A, Petraroli M (2009) A study of the microstructure and hardness of two titanium alloys: Commercially pure and Ti-6Al-4V. J Alloys Compd 486(1):162–167. https://doi.org/10.1016/j.jallcom.2009.06.172
41. TIMET (1999) Corrosion resistance of titanium. https://www.nrc.gov/docs/ML9932/ML993210187.pdf. Accessed 27 Aug 2022
42. Spacht RB (1946) The corrosion resistance of aluminum and its alloys. J Chem Educ 23(5):253. https://doi.org/10.1021/ed023p253
43. Sherif E-S, Abdo H, Alharthi N (2020) Beneficial effects of vanadium additions on the corrosion of Ti6AlxV alloys in chloride solutions. Met—Open Access Metall J 10:264. https://doi.org/10.3390/met10020264
44. Vignesh RV, Padmanaban R, Govindaraju M, Priyadharshini GS (2019) Mechanical properties and corrosion behaviour of AZ91D-HAP surface composites fabricated by friction stir processing. Mater Res Express 6(8):85401. https://doi.org/10.1088/2053-1591/ab1ded
45. Vaira VR, Padmanaban R, Govindaraju M (2020) Synthesis and characterization of magnesium alloy surface composite (AZ91D–SiO_2) by friction stir processing for bioimplants. Silicon 12(5):1085–1102. https://doi.org/10.1007/s12633-019-00194-6
46. Sherif KP, Narayan R (1989) Electrochemical behaviour of aluminium in 1M NaCl solution: part 1: open circuit potential measurements. Br Corros J 24(3):199–203. https://doi.org/10.1179/000705989798270018
47. Ma K, Zhang R, Sun J, Liu C (2020) Oxidation mechanism of biomedical titanium alloy surface and experiment. Int J Corros 2020:1678615. https://doi.org/10.1155/2020/1678615
48. Minh DP, Lyczko N, Sebei H, Nzihou A, Sharrock P (2012) Synthesis of calcium hydroxyapatite from calcium carbonate and different orthophosphate sources: a comparative study. Mater Sci Eng B 177(13):1080–1089. https://doi.org/10.1016/j.mseb.2012.05.007
49. Witte F et al (2005) In vivo corrosion of four magnesium alloys and the associated bone response. Biomaterials 26(17):3557–3563. https://doi.org/10.1016/j.biomaterials.2004.09.049
50. Khanra AK, Jung HC, Yu SH, Hong KS, Shin KS (2010) Microstructure and mechanical properties of Mg-HAP composites. Bull Mater Sci 33(1):43–47. https://doi.org/10.1007/s12034-010-0006-z
51. Vignesh RV, Padmanaban R, Govindaraju M (2019) Investigations on the surface topography, corrosion behavior, and biocompatibility of friction stir processed magnesium alloy AZ91D. Surf Topogr Metrol Prop 7(2):25020. https://doi.org/10.1088/2051-672x/ab269c
52. Zhang Y, Li J, Che S, Tian Y (2020) Electrochemical polishing of additively manufactured Ti-6Al-4V alloy. Met Mater Int 26(6):783–792. https://doi.org/10.1007/s12540-019-00556-0
53. Ramalingam VV, Ramasamy P, Datta M (2019) Microstructure, hardness and corrosion behaviour of friction-stir processed AA5083. Anti-Corrosion Methods Mater 66(6):791–801. https://doi.org/10.1108/ACMM-07-2017-1816